Nanoscale Advances

ROYAL SOCIETY OF CHEMISTRY

PAPER

View Article Online
View Journal | View Issue

Cite this: *Nanoscale Adv.*, 2026, **8**, 3598

$KNbO_3$-based multiferroic heterostructures: a lead-free alternative for strain-driven magnetic modulations

Hemanita Sharma, [ab] Deepak Dagur, [†b] Federico Motti, [b] Aleksandr Yu. Petrov, [b] Prajna Bhatt, [b] Luca Sbuelz, [b] Gian Marco Pierantozzi, [b] Riccardo Cucini, [b] Giorgio Rossi, [bc] Piero Torelli [b] and Giovanni Vinai [*b]

Received 19th March 2026
Accepted 20th May 2026

DOI: 10.1039/d6na00213g

rsc.li/nanoscale-advances

Artificial multiferroic heterostructures offer a versatile platform for engineering magnetic properties through interfacial strain and magnetoelectric coupling. In this framework, we demonstrate the growth of both Ni and $La_{0.67}Sr_{0.33}MnO_3$ ferromagnetic thin films on $KNbO_3$ (100) single crystals. We show, by combining structural and magneto-optical characterizations, how their magnetic responses are affected by the structural transitions taking place in the substrate as a function of temperature. In particular, we observe sensitive modifications in the ferroelectric domain composition of $KNbO_3$, especially after cooling from orthorhombic to rhombohedral phase, leading to a transition from in-plane anisotropic to isotropic magnetization behaviour in Ni thin films. Temperature dependent magnetic characterizations show a coercivity modulation while crossing the structural transition for both Ni and $La_{0.67}Sr_{0.33}MnO_3$ films, signature of interfacial strain-driven coupling. To the best of our knowledge, these are the first reported $KNbO_3$-based multiferroic heterostructures, establishing this lead-free material as a potential functional host for both metallic magnetostrictive and complex oxide thin films.

Introduction

Over the past two decades, the field of multiferroics has undergone a profound transformation driven by advances in thin film synthesis, interface design, and *operando* characterization. Several reviews highlight how the controlled coupling of electric, magnetic, elastic and structural order parameters has shifted multiferroics from niche materials systems toward a central position in functional materials research.[1–4] In particular, the field has recently increased focus on engineered heterostructures in which the driving principle lays in magnetoelectric (ME) interactions at the interface, rather than relying on single-phase compounds where ferroic orders coexist intrinsically yet often weakly, especially from the magnetic point of view.[5,6] In parallel, the broader functionality of ferroic oxides has continued to expand beyond conventional electronic and spintronic applications. Recent studies demonstrate that polarization-driven effects in ferroelectric materials can also influence charge separation, surface chemistry, and catalytic reactivity, further emphasizing the multifunctional nature of these oxide systems and the technological relevance of interfacial polarization control.[7]

Within this framework, artificial multiferroic heterostructures combining ferroelectric (FE) and ferromagnetic (FM) layers have become an important platform for probing nanoscale ME interactions. The integration of a FE material, capable of polarization reversal, with a FM thin layer whose magnetization is highly responsive to interfacial strain, charge modulation, and bonding chemistry enables reversible electrical control of magnetic states with reduced energy consumption.[8–10] These insights highlight the potential of FE/FM heterostructures as a pathway toward compact, low-power spintronic technologies, where interfacial design at the atomic scale governs functionality and device performance.[8,11–15]

FE materials with well-defined structural phase transitions provide an effective platform for tailoring ME coupling in multiferroic heterostructures. Across such transitions, symmetry changes modify polarization stability, dielectric susceptibility, lattice strain, and interfacial screening, all of which can exert strong control over the magnetic configuration of an adjacent FM layer. Theoretical calculations[9,16] as well as experimental results[17–20] show that FE exhibit pronounced enhancements in susceptibility and electromechanical response near phase boundaries, thereby offering intrinsic amplification mechanisms for cross-coupling between ferroic order parameters. Widely used FE substrates such as $BaTiO_3$

[a]*Department of Physics, University of Trieste, Piazzale Europa, 1, Trieste 34127, Italy*
[b]*CNR – Istituto Officina dei Materiali (IOM), Unità di Trieste, Strada Statale 14, km 163.5, 34149 Basovizza, TS, Italy. E-mail: vinai@iom.cnr.it*
[c]*Department of Physics, University of Milan, Via Celoria 16, Milan I-20133, Italy*
† Current address: ALBA Synchrotron, Carrer de la Llum, 2-26, 08290 Cerdanyola del Vallès, Barcelona, Spain.

(BTO)[21] and $[Pb(Mg_{1/3}Nb_{2/3})\text{-}O_3]\text{-}x[PbTiO_3]$ (PMN-xPT)[22,23] are now established platforms for engineering temperature-driven, strain-mediated control of interfacial magnetism. The former provides structural transitions accompanied by pronounced strain discontinuities, and the latter offers exceptionally large piezoelectric coefficients and electrically induced strain. However, several alternative FE materials with similar transitions are still under investigation, leaving room for further explorations, exploiting for instance different temperature ranges and/or lattice parameters.

In this context, potassium niobate ($KNbO_3$, KNO) stands out as a particularly compelling candidate. KNO is a lead-free FE perovskite first synthesized in the 1950s, known for its well-defined sequence of first-order structural transitions, progressing through four crystal symmetries: rhombohedral (R) below ~210 K, orthorhombic (O) (~210–490 K), tetragonal (T) (~490–690 K) followed by cubic (C) paraelectric above ~690 K (see Fig. 1(a)).[24,25] These transitions are accompanied by robust spontaneous polarization, and the overall sequence mirrors that of BTO, with however the orthorhombic phase stable at RT instead of the tetragonal one. Importantly, KNO is lead-free and environmental friendly,[25] offering a sustainable alternative to Pb-based ferroelectrics such as PZT or PMN-PT, fitting well in the family of lead-free piezoceramics.[26] However, its integration in multiferroic heterostructures has been up to now extremely limited and focused on its photocatalytic properties,[27–29] whereas its interfacial coupling with FM materials is to our knowledge unexplored.

Building on these contexts, we explore KNO/Ni and KNO/$La_{0.67}Sr_{0.33}MnO_3$ (LSMO) heterostructures as lead-free systems for ME coupling. Ni thin films serve as model magnetostrictive layer, allowing us to probe the influence of strain modulations driven by FE transitions on the interfacial FM layer. On the other hand, optimally doped LSMO, a strongly correlated FM oxide highly sensitive to lattice variations,[21] provides an oxide-based complementary system whose epitaxial growth requirements are stricter than those of Ni.

In this work, by combining structural and magnetic characterization, we show that KNO (100) is compatible with epitaxial growth of strained ferromagnetic LSMO, whereas magnetostrictive Ni ultrathin films proved to be particularly sensitive to KNO structural transitions. In addition, temperature-driven structural transitions modify the crystalline quality of KNO at RT, which tends to lose its pristine order.

Experimental details

Sample preparation

FM thin films were grown on pristine one-sided polished (100) KNO substrates (2.5 × 2.5 mm^2, thickness 0.5 mm) supplied by SurfaceNet GmbH. Three deposition methods were employed to fabricate the heterostructures. First, 7 nm thick Ni layers were grown by electron beam evaporation at the molecular beam epitaxy (MBE) Cluster of NFFA-Trieste facility[30] at room temperature (RT), at a base pressure below 1×10^{-9} mbar. The Ni film was subsequently capped with a 4 nm thick MgO layer to prevent oxidation (see Fig. 1(c)). In a second approach, additional heterostructures were prepared by sputter deposition of Ni (14 ± 2 nm thick), followed by capping with Al (5 ± 2 nm thick) under a base pressure of 5×10^{-6} mbar. The sputtered heterostructures were first magnetically characterized in pristine state and subsequently annealed at approximately 770 K under Ar gas continuous flow in a controlled environment. Finally, epitaxial thin films of $La_{0.67}Sr_{0.33}MnO_3$ of 40 unit cells

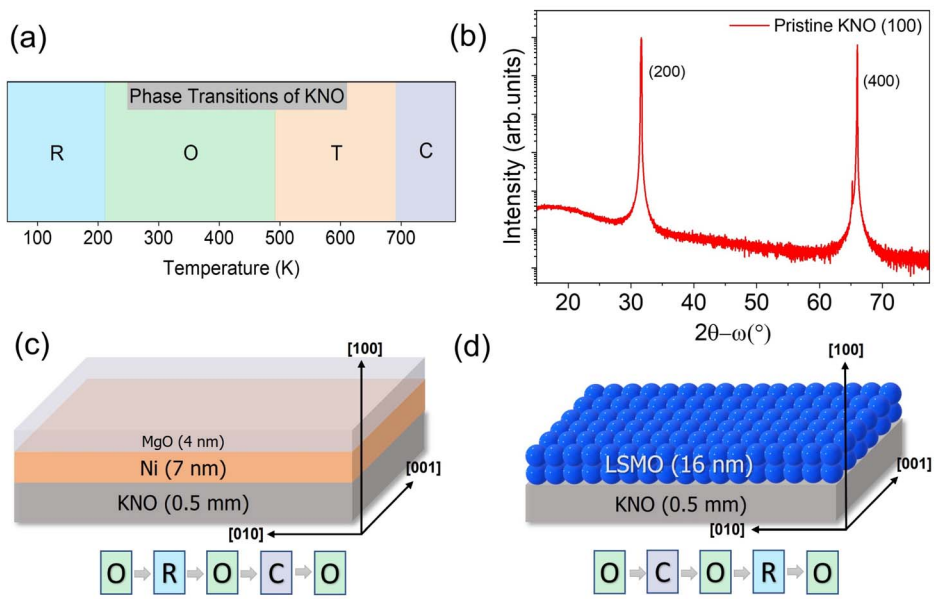

Fig. 1 (a) Temperature-dependent structural phase diagram of KNO crystals, (b) wide 2θ–ω scan of pristine KNO (100) in its orthorhombic phase, (c and d) schematic representation of KNO/Ni (c) and (d) KNO/LSMO heterostructures; below them, the thermal treatments of the two systems are shown.

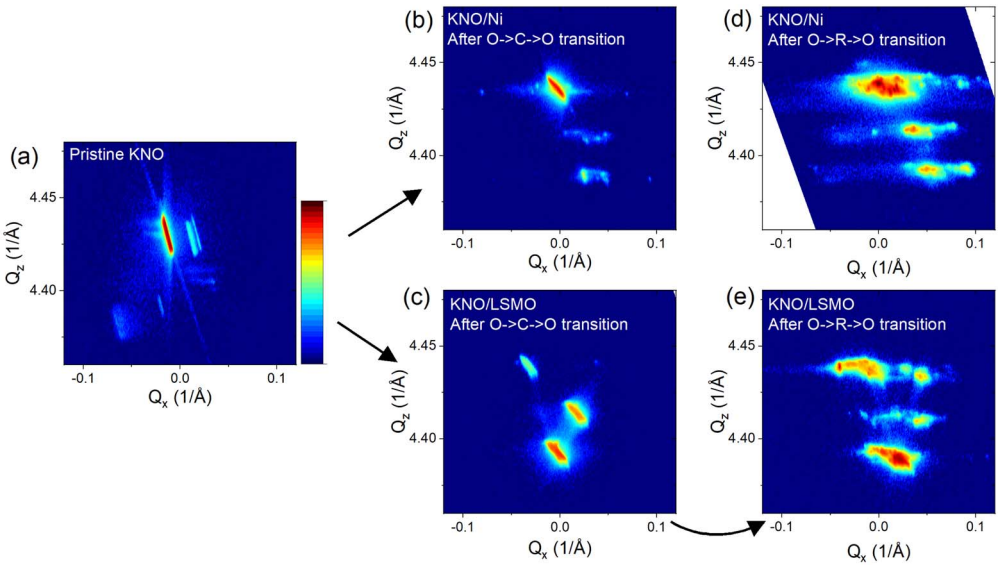

Fig. 2 XRD 2D-RSMs of the (400) Bragg peak of KNO (100) single crystal after thermal treatments: (a) in pristine state; (b) KNO/Ni after heating to C phase; (c) KNO/LSMO after deposition at 1000 K (*i.e.*, heating to C phase); (d) KNO/Ni after cooling to R phase; (e) KNO/LSMO, which passed through O/C/O transition, after cooling to R phase.

(≈16 nm thickness) were grown layer-by-layer using an alternate shutter deposition method in an oxide-molecular beam epitaxy (o-MBE) system operating under ultra-high vacuum conditions (see Fig. 1(d)), at a deposition rate of 1 unit cell per minute.[31] The substrate temperature was maintained at 1000 K during growth (*i.e.* in this cubic phase), under an oxygen partial pressure of 2×10^{-6} mbar.

Magnetic characterizations

Magnetic hysteresis loops were measured by longitudinal MOKE using an s-polarized 658 nm wavelength laser of 8 mW power, with a laser spot size of about 500 μm^2. Coercive field and remanence were evaluated as the averaged half width hysteresis loops at zero magnetization, averaging both negative and positive sides of the loop. Temperature-dependent MOKE measurements were done with the sample in ultra-high vacuum (UHV) condition using a He liquefier closed circuit with a temperature range of ~50–300 K.

Structural characterizations

XRD measurements were performed with X'Pert PANalytical Empyrean diffractometer. Monochromatic Cu-Kα_1 ($\lambda = 1.54056$

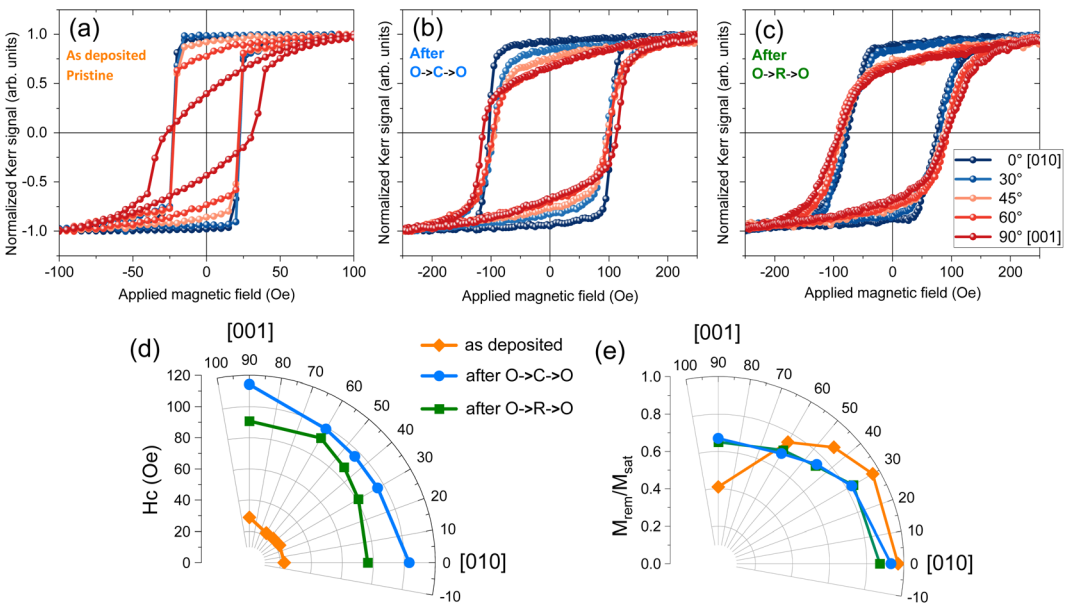

Fig. 3 Angular dependent room temperature MOKE measurements of KNO/Ni heterostructure (a) as deposited (pristine KNO); (b) after heating up to the cubic phase (O– > C– > O); (c) after cooling down to the rhombohedral phase (O– > R– > O). Angular dependence of (d) coercive field (H_C) and (e) remanence (M_{rem}/M_{sat}) in the above cases.

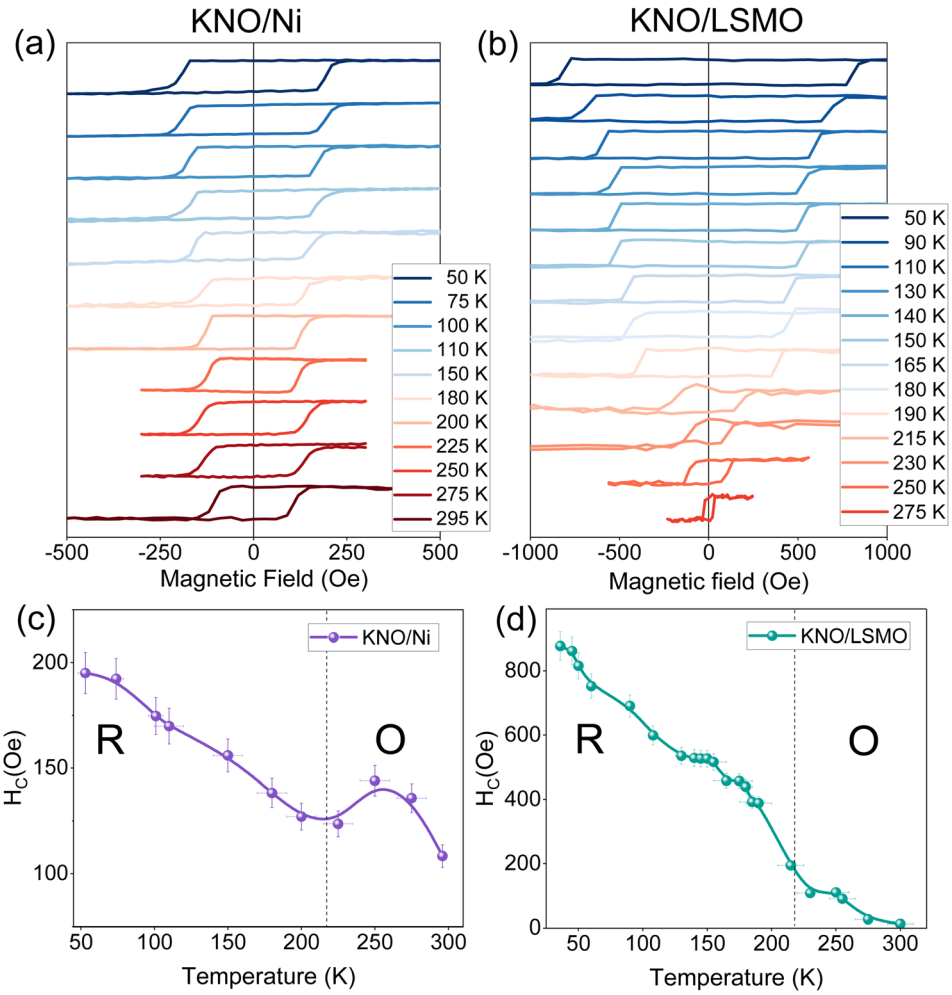

Fig. 4 Temperature dependent MOKE hysteresis loops (a and b) and coercivity *vs.* temperature curves (c and d) for KNO/Ni and KNO/LSMO heterostructures, respectively along [001] direction showing the phase transition of KNO from rhombohedral (R) to orthorhombic (O).

Å) radiation was employed with Hybrid Monochromator 2X Ge (220). It consists of a parabolic shaped graded multilayer (X-ray mirror) and a special channel-cut germanium crystal. We used the divergence slit of 1/4° which controls the height of the X-ray beam coming off the monochromator to be 0.65 mm. A PIXcel^{3D} – Medipix3 detector was used with a scanning area detector (2D) mode.

Results and discussion

The structural analysis of the pristine KNO (100) substrates was first evaluated prior to the deposition of the FM thin films. In agreement with the established phase diagram of KNO (Fig. 1(a)), the substrates exhibited an orthorhombic crystal structure at RT.

From the XRD pattern of the pristine KNO (100) single-crystal substrate measured in symmetric 2θ–ω geometry (Fig. 1(b)) displays two intense diffraction peaks at approximately 31° and 66°. These reflections are characteristic of a well-oriented orthorhombic KNO single crystal at room temperature. In its orthorhombic ferroelectric phase, KNO exhibits slightly unequal lattice parameters arising from the distortion of the perovskite framework associated with spontaneous polarization. As the substrate is cut along the (100) direction, only lattice planes parallel to the surface satisfy the Bragg condition in the out-of-plane scan. Accordingly, the observed peaks can be assigned to the (200) and (400) reflections of orthorhombic KNO. The absence of any additional diffraction features further confirms the phase purity and strong (100) orientation of the substrate, with no detectable secondary phases or misoriented domains. 2D reciprocal space map (RSM) around the KNO (400) reflection exhibits a dominant sharp diffraction peak accompanied by a weaker feature at the same Q_z and slightly shifted along Q_x, indicating the presence of multiple structural variants in the orthorhombic KNO crystal (Fig. 2(a)). The calculated lattice constants are $a = 5.70$ Å from the main peak position, whereas the asymmetric reciprocal space maps allowed us to identify the edges of the sample as the [010] and [001] directions, giving us the lattice constants values $b = 3.97$ Å and $c = 5.73$ Å, which are in excellent agreement with previously reported values for orthorhombic KNO (space group #38, *Bmm*2).[32,33] The polarization direction in orthorhombic KNO is

along *c*, which is in plane for this crystal cut. In the case of KNO/Ni heterostructures, the FM layer depositions were done at RT, so the magnetic characterization of the as-deposited sample corresponds to the pristine structure. The quality of the deposited Ni layer was verified *via* X-ray absorption spectroscopy (XAS) at APE-HE beamline of the NFFA facility at the Elettra Sincrotrone Trieste synchrotron radiation source.[34] The spectrum showed a fully metallic Ni layer, signature of a high quality deposition (see Fig. S1).

Following the structural characterization of pristine KNO (100) substrates, the impact of their phase-transition-driven structural evolution on FM interfacial layers was investigated. As discussed above, Ni films were deposited at room temperature, preserving the orthorhombic phase of KNO, whereas LSMO growth required heating the substrate at 1000 K, driving KNO across its ferroelectric–paraelectric phase transitions. Additionally, the symmetric 2θ–ω XRD scan acquired after LSMO deposition clearly reveals the characteristic (110) reflection of the LSMO thin film together with the (200) reflection of the KNO substrate (Fig. S2(c)), confirming the successful growth of the heterostructure. From the position of the LSMO (110) peak, the corresponding lattice parameter was extracted to be approximately 3.87 Å, consistent with values reported for epitaxial LSMO thin films.[35] The comparatively weak intensity of the LSMO reflection arises from the limited film thickness ($\approx$40 u.c.), which reduces the diffracted intensity while still permitting clear resolution of the film and substrate peaks.

This difference in thermal history provides a natural framework to explore how substrate structural changes and ferroelastic domain reconfiguration influence the magnetic properties of the heterostructures. To isolate the effect of phase transitions, KNO/Ni was heated up to the cubic phase and subsequently cooled down to the rhombohedral phase. For both heterostructures, additional diffraction maxima appear at three distinct Q_z positions after heating (Fig. 2(b) and (c)). Besides the main (400) reflection of KNO, the extra peaks correspond to the reflections that can be indexed as (222) and (004), as determined from the calculated lattice vectors ($Q_z = 4.4397$ Å^{-1} and $Q_z = 4.413$ Å^{-1}, respectively), indicating the formation of multiple FE domain variants associated with different orientations of the spontaneous polarization. These variants stabilize distinct orthorhombic lattice configurations upon cooling, while largely preserving long-range crystalline coherence, as reflected by the relatively narrow diffraction features. Finally, a markedly different structural response is observed after cooling to the rhombohedral phase, where the RSMs exhibit broadened and multiple diffraction features for both heterostructures, indicating the formation of multiple FE domain variants and increased structural heterogeneity (Fig. 2(d) and (e)). Although intensity remains distributed across three Q_z values, the diffraction features broaden significantly along Q_x and develop a more complex profile, reflecting a wider distribution of structural variants. The rhombohedral-to-orthorhombic transition therefore introduces substantial lattice distortions and strain gradients, which perturb the epitaxial coherence of the substrate and are expected to be transferred to the overlying ferromagnetic layers. Such strain transfer across the interface constitutes a key mechanism of magnetoelectric coupling in FE/FM heterostructures, whereby lattice distortions modulate the magnetic anisotropy of the ferromagnetic films, and it will be shown in the following that this holds also in the case of KNO-based ones.

As a final note, particular caution has to be taken when handling KNO crystals along the characterization processes. Despite their high structural quality, KNO substrates were found to be rather mechanically fragile, since even mild mechanical contact led to perceptible surface deformations. This can justify the degree of variability of the RSMs measured on the two heterostructures after structural transitions. However, despite the fact that the diffraction patterns present differences between the two systems, the trend observed after the structural transitions is consistent for both cases.

To directly probe the interfacial coupling, longitudinal MOKE measurements were performed on both heterostructures. For KNO/LSMO, measurements at RT after deposition proved to be challenging, as the very soft ferromagnetic character of ultrathin LSMO results in an almost negligible coercive field and an extremely weak Kerr signal, most probably due to of a Curie temperature close to RT, as it will be shown in the following discussions, therefore preventing a reliable determination of angular-dependent anisotropy.[21] In contrast, the as-deposited KNO/Ni heterostructure was characterized at RT in both pristine state and after heating and cooling cycles through KNO structural transitions. On pristine KNO, Ni exhibits a pronounced in-plane uniaxial magnetic anisotropy, as evidenced by the angular dependence of the hysteresis loops, coercive field, and remanent magnetisation (Fig. 3(a)). The magnetic easy axis is aligned close to the [010] crystallographic direction, demonstrating that the orthorhombic structural order of the KNO substrate is imprinted onto the magnetic response of Ni, evidencing a strong magnetoelastic coupling between the substrate lattice and the FM film. Angular-dependent longitudinal MOKE measurements were performed on pristine KNO/Ni heterostructures prepared by both electron-beam evaporation and sputtering. In both cases, the angular dependence of the coercive field and remanent magnetization exhibits a similar anisotropic behaviour, with nearly identical positions of easy [010] and hard [001] axes (see SI, Fig. S3). This demonstrates that Ni films grown on KNO develop comparable magnetic anisotropy irrespective of the deposition method, highlighting KNO as a compatible FE substrate for the fabrication of artificial multiferroic heterostructures. Thermal cycling across the structural phase transitions of KNO leads to clear modifications of the magnetic anisotropy in KNO/Ni, highlighting the sensitivity of the FM layer to substrate symmetry and strain evolution. After heating KNO/Ni to the cubic phase and cooling back to RT (Fig. 3(b)), the magnetic properties change noticeably. This behaviour reflects the domain reorganisation of the KNO substrate during the O $\rightarrow$ C $\rightarrow$ O transition, where multiple FE domain variants are formed, as evidenced by the 2D-RSM (Fig. 2(b)). The coexistence of these domains leads to different local strain at the interface, meaning that the Ni layer no longer experiences a single, well-defined orthorhombic distortion. Consequently, a more isotropic

behaviour is observed, with an easy axis less defined and a marked increase of coercivity. A more pronounced structural modification occurs when KNO/Ni is cycled through the rhombohedral phase (O → R → O). In this case, the 2D-RSM after cooling (Fig. 2(d)) indicates a much more disordered FE domain configuration, leading to a highly heterogeneous interfacial strain, which results again in an almost isotropic anisotropy of the interfacial Ni layer (Fig. 2(c)). These angular dependences are summarized on the polar plots of coercivity and remanence ratio in Fig. 3(d) and (e).

Temperature dependent MOKE measurements offer further evidence of this interfacial coupling mechanism (Fig. 4). In the KNO/Ni heterostructure, the coercive field H_C along the [010] direction reveals a sharp upturn, with an increase of its value as the substrate transitions from the orthorhombic to the rhombohedral phase (Fig. 4(a) and (c)). This behaviour directly reflects the sensitivity of the magnetic film to the underlying structural deformation. On the other hand, the epitaxial strain and the reduced thickness of the LSMO layer suppress its Curie temperature, which is found at ∼270–280 K. In this case, in correspondence to the KNO structural transition we observe a marked decrease of H_C, which can be attributed to a combination of the approaching T_C and to strain-driven interfacial coupling (Fig. 4(b) and (d)). Ultimately, however in different ways, both heterostructures present magnetic modulations in correspondence to the structural evolution of the KNO substrate. Collectively, these findings demonstrate that the structural evolution of ferroelectric KNO plays a decisive role in governing the magnetic and structural responses of KNO/FM systems, providing compelling evidence of strain-mediated ME coupling at the interface.

Finally, wavelength-dependent photocurrent measurements were performed on KNO/Ni using an optical parametric amplifier (OPA) setup. A clear photocurrent was detected in the near-UV-visible range, with a maximum at ∼385 nm, in good correspondence with the bandgap of KNO (∼3.2–3.4 eV).[24,25,36] Additionally, when illuminated with a constant wavelength of 405 nm, a stable photocurrent of ∼6 nA emerged, indicating a robust and reversible photo-response, significantly larger than what reported on equivalent PMN-$_{0.4}$PT-based heterostructure, demonstrating efficient photocarrier generation (see SI, Fig. S4).[36,37]

Conclusions

In this work, we have successfully grown high-quality multiferroic heterostructures by integrating epitaxial Ni and LSMO thin films on KNO (100) crystals, up to now unreported in literature. Our results demonstrate that the functional properties of the heterostructures are governed by a strong interplay between the phase-transition-driven structural evolution of the ferroelectric substrate and the magnetic response of the ferromagnetic layers. By combining XRD 2D-RSM with temperature-dependent MOKE measurements, we establish a correlation between the structural modifications of KNO, especially the reconfiguration of FE domains at room temperature, and the modulation of FM anisotropy of interfacial Ni film. Such strain emerges as the dominant mechanism controlling magnetic anisotropy and coercivity in the FM films, since both KNO/Ni and KNO/LSMO heterostructures present coercivity variations in correspondence to the rhombohedral to orthorhombic transition of KNO. This result stimulates for further investigations in magnetostrictive interfacial coupling on KNO-based heterostructures.

Author contributions

Hemanita Sharma: investigation, data curation, methodology, writing – original draft. Deepak Dagur: conceptualization, methodology, validation. Federico Motti: visualization, validation, investigation Aleksandr Yu. Petrov: investigation, validation. Prajna Bhatt: visualization, validation. Luca Sbuelz: investigation. Gian Marco Pierantozzi: investigation, validation. Riccardo Cucini: validation. Giorgio Rossi: resources, project administration. Piero Torelli: supervision. Giovanni Vinai: conceptualization, methodology, validation, writing – review & editing.

Conflicts of interest

No potential conflict of interest was reported by the authors.

Data availability

Data for this article are available at Zenodo at https://doi.org/10.5281/zenodo.19111563

Supplementary information (SI): XAS scan at Ni L2,3 edges on KNO/Ni heterostructures, RHEED and XRD scans of KNO/LSMO heterostructures, angular dependent room temperature MOKE measurements on KNO/Ni heterostructures, deposited either *via* sputtering or electron beam evaporation, and photocurrent measurements. See DOI: https://doi.org/10.1039/d6na00213g.

Acknowledgements

This work was performed in the framework of the Nanoscience Foundry and Fine Analysis (NFFA-MUR Italy Progetti Internazionali) project (https://www.trieste.nffa.eu/). Federico Motti acknowledges fundings from the European Union's Horizon 2020 Research and Innovation Program under Project SINFONIA (grant no. 964396), and from Italian Ministero dell'Università e della Ricerca through the program NEST (project no.: PE0000021). The authors thank Andrea Fondacaro for technical support.

References

1 H. Schmid, *Ferroelectrics*, 1994, **162**, 317–338.
2 W. Eerenstein, N. D. Mathur and J. F. Scott, *Nature*, 2006, **442**, 759–765.
3 D. Khomskii, *Physics*, 2009, **2**, 20.
4 M. Fiebig, T. Lottermoser, D. Meier and M. Trassin, *Nat. Rev. Mater.*, 2016, **1**, 16046.

5 T. Taniyama, Y. Gohda, K. Hamaya and T. Kimura, *Sci. Technol. Adv. Mater.*, 2024, **25**, 2412970.
6 C. A. F. Vaz, *J. Phys. Condens. Matter*, 2012, **24**, 333201.
7 H. Khan and T. Ahmad, *J. Phys. Mater.*, 2026, **9**, 012001.
8 J. T. Heron, J. L. Bosse, Q. He, Y. Gao, M. Trassin, L. Ye, J. D. Clarkson, C. Wang, J. Liu, S. Salahuddin, D. C. Ralph, D. G. Schlom, J. Íñiguez, B. D. Huey and R. Ramesh, *Nature*, 2014, **516**, 370–373.
9 D. Damjanovic, *Rep. Prog. Phys.*, 1998, **61**, 1267–1324.
10 F. Cucchiella, I. D'Adamo, S. C. Lenny Koh and P. Rosa, *Renew. Sustain. Energy Rev.*, 2015, **51**, 263–272.
11 R. Ramesh and S. Manipatruni, *Proc. R. Soc. A Math. Phys. Eng. Sci.*, 2021, **477**, 27097791.
12 R. Ramesh and N. A. Spaldin, *Nat. Mater.*, 2007, **6**, 21–29.
13 Z. Huang, Ariando, X. Renshaw Wang, A. Rusydi, J. Chen, H. Yang and T. Venkatesan, *Adv. Mater.*, 2018, **30**, 1802439.
14 H. Ohno, M. D. Stiles and B. Dieny, *Proc. IEEE*, 2016, **104**, 1782–1786.
15 S. Manipatruni, D. E. Nikonov, C. C. Lin, T. A. Gosavi, H. Liu, B. Prasad, Y. L. Huang, E. Bonturim, R. Ramesh and I. A. Young, *Nature*, 2019, **565**, 35–42.
16 J. F. Scott, *Science*, 2007, **315**, 954–959.
17 J. H. Haeni, *et al.*, *ChemInform*, 2004, **35**, 583–586.
18 E. Sun and W. Cao, *Prog. Mater. Sci.*, 2014, **65**, 124–210.
19 T. Bayaraa, Y. Yang, M. Ye and L. Bellaiche, *Phys. Rev. B*, 2021, **103**, L060103.
20 S. Sahoo, S. Polisetty, C. G. Duan, S. S. Jaswal, E. Y. Tsymbal and C. Binek, *Phys. Rev. B: Condens. Matter Mater. Phys.*, 2007, **76**, 092108.
21 F. Motti, G. Vinai, A. Petrov, B. A. Davidson, B. Gobaut, A. Filippetti, G. Rossi, G. Panaccione and P. Torelli, *Phys. Rev. B*, 2018, **97**, 094423.
22 D. Dagur, V. Polewczyk, A. Y. Petrov, P. Carrara, M. Brioschi, S. Fiori, R. Cucini, G. Rossi, G. Panaccione, P. Torelli and G. Vinai, *Adv. Mater. Interfaces*, 2022, **9**, 2201337.
23 D. Dagur, A. M. Finardi, V. Polewczyk, A. Y. Petrov, S. Dolabella, F. Motti, H. Sharma, E. Dobovicnik, A. Giugni, G. Rossi, C. Fasolato, P. Torelli and G. Vinai, *ACS Appl. Electron. Mater.*, 2024, **6**, 6648–6656.
24 G. Shirane, H. Danner, A. Pavlovic and R. Pepinsky, *Phys. Rev.*, 1954, **93**, 672–673.
25 D. Wang, G. Wang, Z. Lu, Z. Al-Jlaihawi and A. Feteira, *Front. Mater.*, 2020, **7**, 91.
26 Y. Saito, H. Takao, T. Tani, T. Nonoyama, K. Takatori, T. Homma, T. Nagaya and M. Nakamura, *Nature*, 2004, **432**, 84–87.
27 U. Farooq, P. Chaudhary, P. P. Ingole, A. Kalam and T. Ahmad, *ACS Omega*, 2020, **5**, 20491–20505.
28 J. Zhang, L. Du, J. Chen, J. Tan, X. Bai, Y. Chen and J. Zhu, *Ceram. Int.*, 2024, **50**, 31737–31743.
29 F. Liu, P. Li, Z. Du, L. Lan, H. Xie, Y. Dan, Y. Huang and L. Jiang, *ACS Appl. Mater. Interfaces*, 2024, **16**, 69418–69429.
30 G. Vinai, F. Motti, A. Y. Petrov, V. Polewczyk, V. Bonanni, R. Edla, B. Gobaut, J. Fujii, F. Suran, D. Benedetti, F. Salvador, A. Fondacaro, G. Rossi, G. Panaccione, B. A. Davidson and P. Torelli, *Rev. Sci. Instrum.*, 2020, **91**, 085109.
31 B. A. Davidson, A. Yu. Petrov, F. Li, R. Pons, P. Sosa-Lizama, H. Shin, C. Liu, P. Parisse, P. Torelli, G. Cristiani, Y. E. Suyolcu, P. A. van Aken, G. Logvenov, G. Kim, X. Xi, E. Benckiser and K. Zou, *Nat. Commun.*, 2025, **16**, 8587.
32 P. D. Han, D. A. Payne, A. G. Kalinichev, J. D. Bass and C. S. Zha, *J. Appl. Phys.*, 1993, **74**, 6603–6608.
33 J. You, G. Li, S. Zhang, X. Zhang, J. Luo, M. Rao and Z. Peng, *J. Alloys Compd.*, 2021, **882**, 160641.
34 G. Panaccione, I. Vobornik, J. Fujii, D. Krizmancic, E. Annese, L. Giovanelli, F. MacCherozzi, F. Salvador, A. De Luisa, D. Benedetti, A. Gruden, P. Bertoch, F. Polack, D. Cocco, G. Sostero, B. Diviacco, M. Hochstrasser, U. Maier, D. Pescia, C. H. Back, T. Greber, J. Osterwalder, M. Galaktionov, M. Sancrotti and G. Rossi, *Rev. Sci. Instrum.*, 2009, **80**, 043105.
35 L. Ye, D. Zhang, J. Lu, S. Xu, R. Xu, J. Fan, R. Tang, H. Wang, H. Guo, W. Li and H. Yang, *J. Phys. D Appl. Phys.*, 2022, **55**, 224002.
36 C. L. Diao and H. W. Zheng, *J. Mater. Sci. Mater. Electron.*, 2015, **26**, 3108–3111.
37 S. H. Wemple and M. DiDomenico, *Phys. Rev. B*, 1971, **3**, 1338–1351.